

# Topological phonons in oxide perovskites controlled by light

Bo Peng,<sup>1</sup> Yuchen Hu,<sup>1,2</sup> Shuichi Murakami<sup>3,4</sup>,  
Tiantian Zhang,<sup>3,4\*</sup> Bartomeu Monserrat<sup>1,5†</sup>

<sup>1</sup>Cavendish Laboratory, University of Cambridge,  
J. J. Thomson Avenue, Cambridge CB3 0HE, United Kingdom

<sup>2</sup>Department of Chemistry, University of Cambridge,  
Lensfield Road,, Cambridge CB2 1EW, United Kingdom

<sup>3</sup>Department of Physics, Tokyo Institute of Technology,  
Ookayama, Meguro-ku, Tokyo 152-8551, Japan

<sup>4</sup>Tokodai Institute for Element Strategy, Tokyo Institute of Technology,  
Nagatsuta, Midori-ku, Yokohama, Kanagawa 226-8503, Japan

<sup>5</sup>Department of Materials Science and Metallurgy, University of Cambridge,  
27 Charles Babbage Road, Cambridge CB3 0FS, United Kingdom

\*†To whom correspondence should be addressed;

E-mail: \* ttzhang@stat.phys.titech.ac.jp; † bm418@cam.ac.uk

**Perovskite oxides exhibit a rich variety of structural phases hosting different physical phenomena that generate multiple technological applications. We find that topological phonons – nodal rings, nodal lines, and Weyl points – are ubiquitous in oxide perovskites in terms of structures (tetragonal, orthorhombic, and rhombohedral), compounds (BaTiO<sub>3</sub>, PbTiO<sub>3</sub>, and SrTiO<sub>3</sub>), and external conditions (photoexcitation, strain, and temperature). In particular, in the tetragonal phase of these compounds all types of topological phonons**

**can simultaneously emerge when stabilized by photoexcitation, whereas the tetragonal phase stabilized by thermal fluctuations only hosts a more limited set of topological phonon states. Additionally, we find that the photoexcited carrier concentration can be used to tune the topological phonon states and induce topological transitions even without associated structural phase changes. Overall, we propose oxide perovskites as a versatile platform in which to study topological phonons and their manipulation with light.**

## **Introduction**

In the family of topological materials, semimetals have an important place in the study of topological order because they exhibit topologically protected surface states (*1*), an anomalous bulk transport phenomenon known as the “quantum anomaly” (*2, 3*), diversified classifications like nodal rings and lines (*4–6*) and Weyl and Dirac points (*7–11*), and they serve as a platform for obtaining various other topological states, such as topological (crystalline) insulators (*12*) and Chern insulators (*13*). Beyond electronic structures, topological degeneracies in the spectra of other quasiparticles such as excitons, magnons, and phonons, have drawn wide attention in the past decade (*14–18*). One advantage of the latter group is that excitation of these quasiparticles depends only on the energy of the external probe, rather than being restricted to the bands near the Fermi level like in the case of electrons. Among these quasiparticles, phonons are of particular interest as basic emergent bosonic excitations associated with lattice vibrations (*19–24*), and contribute to many physical processes, such as conventional superconductivity (*25, 26*) and the thermal Hall effect (*27–30*). Thus, studies of topological phonons, and especially on the control of topological phonons, are becoming an important field in condensed matter physics.

Oxide perovskites have gained popularity as a material system in the past decades due to hosting multiple competing phases including ferroelectric (*31*), magnetic (*32*), or superconduct-

ing (26), and also exotic excitations such as skyrmions (33, 34). Additionally, these competing phases are particularly sensitive to external stimuli, including temperature (35), strain (36), pressure (37), and composition (38). More recently, theoretical and experimental evidence has demonstrated that light is yet another means by which it is possible to control the crystal symmetry of perovskites (39–43). As topological order is intimately related to symmetry, the versatility of the perovskite family makes these structures promising platforms to also explore topological properties. However, most oxide perovskites are large gap insulators (for example  $\text{BaTiO}_3$ ,  $\text{SrTiO}_3$ , and  $\text{PbTiO}_3$ ), and as a consequence they exhibit no electronic topological states.

In this work, we show that the phonon spectrum of multiple noncentrosymmetric perovskites can host three types of topological states: topological nodal rings, nodal lines, and Weyl points; suggesting that topological phonons are pervasive in different structural phases of oxide perovskites. Using the tetragonal  $\text{BaTiO}_3$  phase as a prototype, we show that all these types of topological phonon emerge simultaneously when this phase is stabilized by photoexcitation. Additionally, topological order can be controlled with the photoexcited carrier density, driving topological transitions without any associated structural phase change, including the creation and annihilation of Weyl phonons and switching between nodal-ring and nodal-line phonons. In contrast, when the tetragonal phase of  $\text{BaTiO}_3$  is stabilized by thermal fluctuations, it only exhibits a more limited number of topological states. This is because the long-range Coulomb interaction leads to a large energy splitting between the longitudinal and transverse optical phonons (LO-TO splitting), reducing the possibility of topological degeneracies between these bands. The photoexcitation route eliminates this problem because photoexcited carriers can screen long-range interactions.

## Results

### Crystal structures and structural phase transitions in BaTiO<sub>3</sub>

As one of the most studied perovskite materials, BaTiO<sub>3</sub> has a cubic ABO<sub>3</sub>-type crystal structure at temperatures above 393 K, with the A cation (Ba<sup>2+</sup>) at the corners and the B cation (Ti<sup>4+</sup>) at the center of an octahedral cage of oxygen atoms. Upon cooling, BaTiO<sub>3</sub> undergoes an inversion symmetry-breaking phase transition, giving rise to a tetragonal phase with a deformation along the [001] direction (44). As shown in Fig. 1(a), the phase transition breaks inversion symmetry by the polar displacements of Ti and O atoms along the  $z$  direction, which changes the space group from  $Pm\bar{3}m$  (No. 221) to  $P4mm$  (No. 99). With further cooling, an orthorhombic  $Amm2$  phase appears below 278 K and a rhombohedral  $R\bar{3}m$  phase follows below 183 K. As a result of these temperature-driven phase transitions, the room temperature tetragonal phase exhibits imaginary harmonic phonon modes, as shown in Fig. 1(b). The inclusion of anharmonic vibrations (45) stabilizes the tetragonal structure at 300 K, also shown in Fig. 1(b).

In addition to temperature, multiple strategies have traditionally been proposed to control structural phase transitions in perovskites, including strain (36), pressure (32, 37), and composition (38). More recently, it has been shown that photoexcitation provides an alternative route to stabilizing multiple perovskite phases (39–43). Photoexcitation is relatively economical, and can be easier to control compared to other strategies such as heating to change temperature, material synthesis to change composition or strain, or external pressure. Inspired by these recent discoveries, we find that photoexcitation can also stabilize the imaginary phonon modes of the tetragonal phase of BaTiO<sub>3</sub>: Fig. 1(c) shows that the double well potential energy curve along the imaginary phonon mode of amplitude  $Q$  at the  $\Gamma$  point becomes a single well upon illumination, indicating the stabilization of the crystal structure. The underlying physics is that changing the carrier concentration  $n$  induced by photoexcitation leads to changes in the potential energy

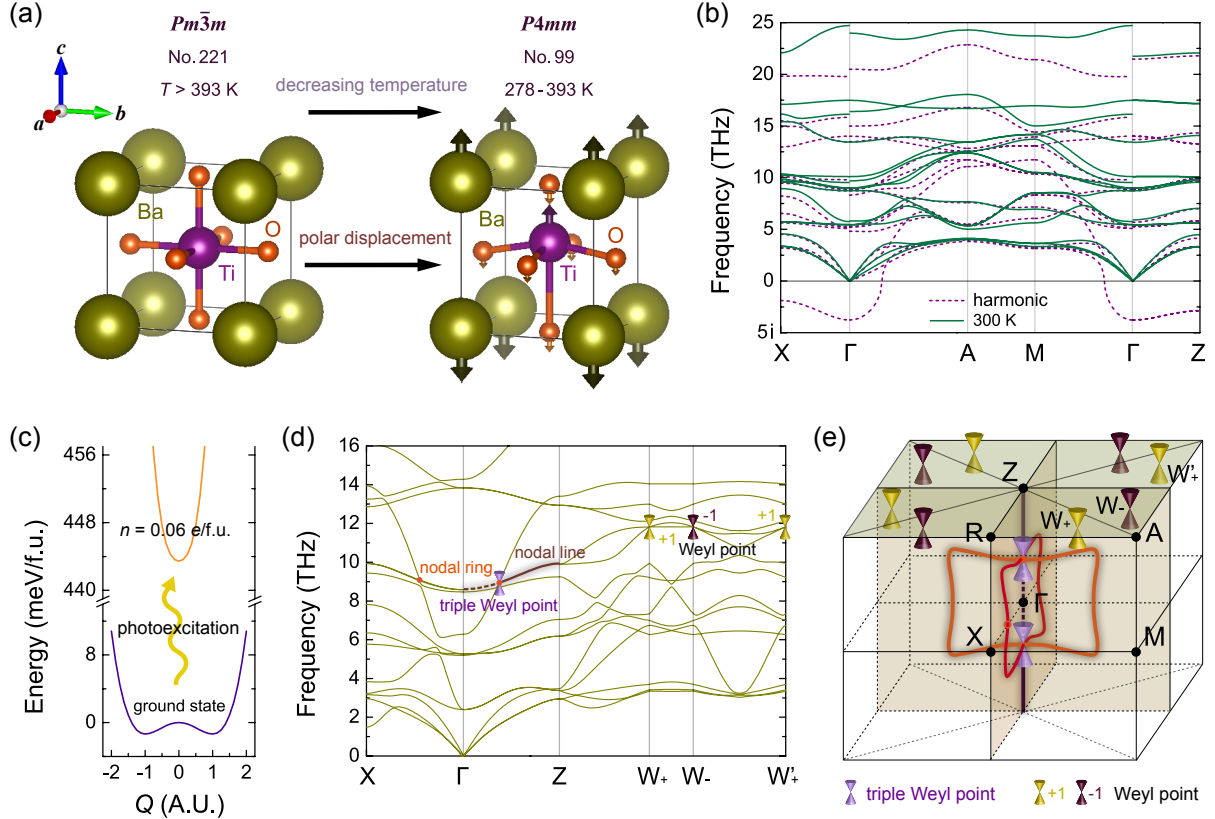


**Figure 1: Crystal structure and phonon dispersion of tetragonal BaTiO<sub>3</sub>.** (a) Crystal structures of the high-temperature cubic phase (No. 221,  $Pm\bar{3}m$ ) and of the room-temperature tetragonal phase (No. 99,  $P4mm$ ) of BaTiO<sub>3</sub>. (b) Phonon dispersion of tetragonal BaTiO<sub>3</sub> at the harmonic level and at 300 K including anharmonic vibrations. (c) Ground-state and excited-state potential energy surfaces along the  $\Gamma$  point phonon mode that is imaginary within the harmonic approximation. (d) Phonon dispersion of tetragonal BaTiO<sub>3</sub> at  $n = 0.06$  e/f.u. (e) Bulk Brillouin zone at  $n = 0.06$  e/f.u. with two nodal rings on the  $q_x = 0$  and  $q_y = 0$  mirror planes (orange circles, formed by the 10<sup>th</sup> and 11<sup>th</sup> bands), one nodal line along the  $\Gamma$ -Z high-symmetry line (brown line, formed by the 10<sup>th</sup> and 11<sup>th</sup> bands), one pair of triple Weyl points at the intersection points between the nodal rings and nodal line (violet cones, formed by the 10<sup>th</sup>, 11<sup>th</sup> and 12<sup>th</sup> bands), and four pairs of Weyl points on the  $q_z = \pi$  plane (purple and yellow cones, formed by the 10<sup>th</sup> and 11<sup>th</sup> bands).

experienced by the ions, which in turn changes the interatomic force constants and the phonon dispersion. For  $0.04 < n < 0.10$  e/f.u., the  $P4mm$  phase is not only dynamically stable, but it is also thermodynamically more stable than the cubic  $Pm\bar{3}m$  phase; whereas for  $n > 0.10$  e/f.u., the  $P4mm$  phase relaxes to the cubic phase as the latter becomes thermodynamically more stable (39). The relative energy between the two phases and their corresponding lattice constants under illumination are shown in the Supplementary Materials. Figure 1(d) shows the phonon dispersion with a photoexcited carrier density of  $n = 0.06$  e/f.u., confirming the dynamical stabilization of the tetragonal phase.

## Topological phonons in BaTiO<sub>3</sub>

As a large gap insulator, BaTiO<sub>3</sub> displays trivial topology in its electronic band structure [Fig. 2(a)]. However, there are three types of topological states in its phonon dispersion, which are nodal rings, nodal lines, and Weyl points. Since the unit cell of tetragonal BaTiO<sub>3</sub> has 5 atoms, there are 15 branches in the phonon spectrum. Band inversion between the 10<sup>th</sup> and 11<sup>th</sup> bands (labelled by increasing energy) along the X- $\Gamma$  high-symmetry line is protected by  $M_x$  symmetry, which restricts the band crossing to a 1D continuous ring/line on the mirror-invariant plane (46). Therefore a nodal ring is formed on the  $q_x = 0$  plane. Because of the existence of an additional  $C_{4z}$  symmetry, there is another nodal ring located on the  $q_y = 0$  plane, related to the one on the  $q_x = 0$  plane by  $C_{4z}$  symmetry [orange circles in Fig. 1(e)]. The combination of  $C_{4z}$  and mirror symmetries also brings out another type of topological phonon in BaTiO<sub>3</sub>: an endless nodal line along the  $\Gamma$ -Z direction [brown line in Fig. 1(e)]. Intersection points between these two nodal rings and the nodal line form two triple Weyl points located along the Z'(0,0,- $\pi$ )- $\Gamma$ -Z(0,0, $\pi$ ) line. Another topological feature of the band crossings between the 10<sup>th</sup> and 11<sup>th</sup> bands are eight Weyl points on the  $q_z = \pi$  plane [purple and yellow cones in Fig. 1(e)]. These eight Weyl points, located at generic momenta on the  $q_z = \pi$  plane, are not protected by any crystalline

symmetry due to the breaking of the  $M_z$  symmetry in the tetragonal lattice, so we need to apply more advanced symmetry-based indicator theory to diagnose the topology.

To gain a better understanding of the topological nature of the eight Weyl points present in photoexcited tetragonal BaTiO<sub>3</sub>, we explore the existence of Weyl points from the perspective of topology as shown in Fig. 3(a), diagnosing topological degeneracies by using symmetry-based indicators from subgroups (47–49). After obtaining the symmetry data at  $\Gamma$ , M, and X, we note that the symmetry-indicator group for space group No. 99 is a trivial one, and the symmetry data at high-symmetry momenta does not satisfy the compatibility condition. Thus, we need to find a subgroup that has a nontrivial symmetry-based indicator group and satisfies the compatibility condition (23, 50). Space group No. 99 has five subgroups with the same size of unit cell, namely No. 75 ( $P4$ ), No. 25 ( $Pmm2$ ), No. 6 ( $Pm$ ), No. 3 ( $P2$ ), and No. 1 ( $P1$ ). Among them, No. 3 is the maximal subgroup that has a nontrivial symmetry-based indicator group  $\mathbb{Z}_2$  and satisfies the compatibility condition. Thus, subgroup No. 3 is used for further diagnosis. Space group No. 3 only has a generator of  $C_{2z}$  rotation symmetry, so the symmetry-based indicator group  $\mathbb{Z}_2$  corresponds to the  $z_2$  Berry phase of the loop enclosing half of the  $q_z = 0$  [ $X(\pi, 0, 0)$ - $M(\pi, \pi, 0)$ - $M'(-\pi, \pi, 0)$ - $X'(-\pi, 0, 0)$ - $X(\pi, 0, 0)$ ] or  $q_z = \pi$  [ $R(\pi, 0, \pi)$ - $A(\pi, \pi, \pi)$ - $A'(-\pi, \pi, \pi)$ - $R'(-\pi, 0, \pi)$ - $R(\pi, 0, \pi)$ ] plane. If  $z_2 = 0$ , there will be  $0 \bmod 4$  Weyl points on the  $q_z = 0$  and  $q_z = \pi$  planes. Our calculations deliver eight Weyl points in total, corresponding to the case  $\mathbb{Z}_2 = 0$ . Furthermore, considering the additional mirror symmetries in space group No. 99, the eight Weyl points on the  $q_z = \pi$  plane are related by  $M_x$  and  $M_y$  symmetries: four of them with left-hand chirality, while the other four with right-hand chirality.

## Controlling topological phonons by light

As discussed above, both photoexcitation with  $0.04 < n < 0.10$  e/f.u. and temperatures between 278-393 K can stabilize the tetragonal phase of BaTiO<sub>3</sub>, as shown in Figs. 1(b) and (d).

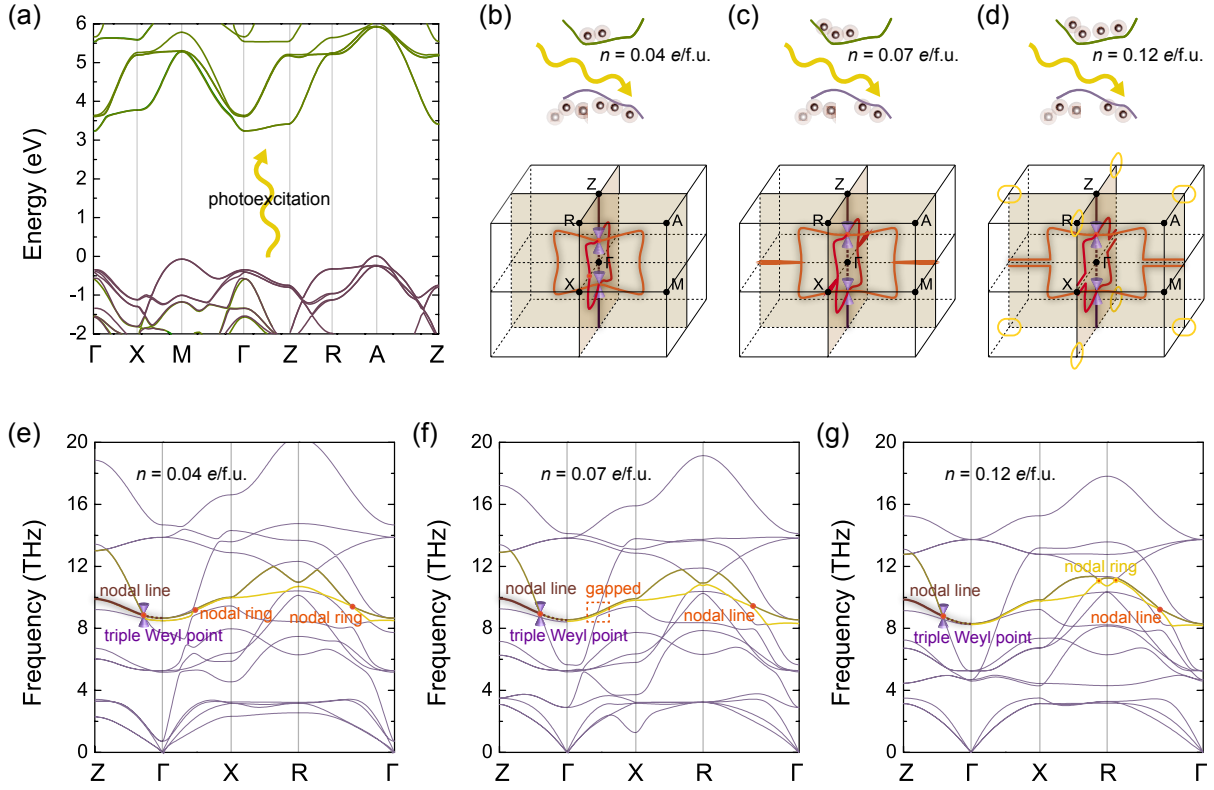


**Figure 2: Nodal lines and nodal rings in tetragonal  $\text{BaTiO}_3$  controlled by light.** (a) Schematic of the photoexcitation process in tetragonal  $\text{BaTiO}_3$ . (b)-(d) Nodal lines and nodal rings formed by the 10<sup>th</sup> and 11<sup>th</sup> phonon branches in the bulk Brillouin zone for photoexcited carrier concentrations of 0.04 e/f.u., 0.07 e/f.u., and 0.12 e/f.u. The corresponding phonon dispersions are shown in (e)-(g).

However, a main difference is that without photoexcitation, the long-range Coulomb interaction leads to a large LO-TO splitting (51), which tends to lift band degeneracies, as shown in Fig. 1(b). Consequently, the eight conventional Weyl points and the two triple Weyl points that we find in illuminated  $\text{BaTiO}_3$  are not observed in temperature-stabilized tetragonal  $\text{BaTiO}_3$  at 300 K (although the presence of nodal-line and nodal-ring phonons is confirmed in the Supplementary Materials). In contrast, under illumination, the photoexcited carriers lead to a strong free-carrier screening that suppresses the LO-TO energy splitting and facilitates the appearance of Weyl phonons in tetragonal  $\text{BaTiO}_3$ . Another advantage of the photoexcitation route is



that, as discussed next, it can drive the phononic system between different topological quantum states, including switching between nodal-ring and nodal-line phonons, controlling the position of Weyl points in momentum space, and creating and annihilating these topological states.

As discussed above, changing the photoexcited carrier density brings about not only the transition between nodal rings and nodal lines, but also the creation of new nodal rings. As shown in Fig. 2(b)-(c), increasing the photoexcited carrier density from  $n = 0.04$  e/f.u. to  $n = 0.07$  e/f.u. drives the two nodal rings to become two nodal lines, and the corresponding phonon spectra are shown in Fig. 2(e)-(f). Further increasing  $n$  to 0.12 e/f.u. (under which conditions the tetragonal structure becomes cubic) leads to the formation of two nodal rings around the R point on the  $q_x = 0$  and  $q_y = 0$  planes, as shown in Fig. 2(d) and (g). Thus, by changing  $n$ , nodal rings in the phonon spectra can be created or transformed into nodal lines.

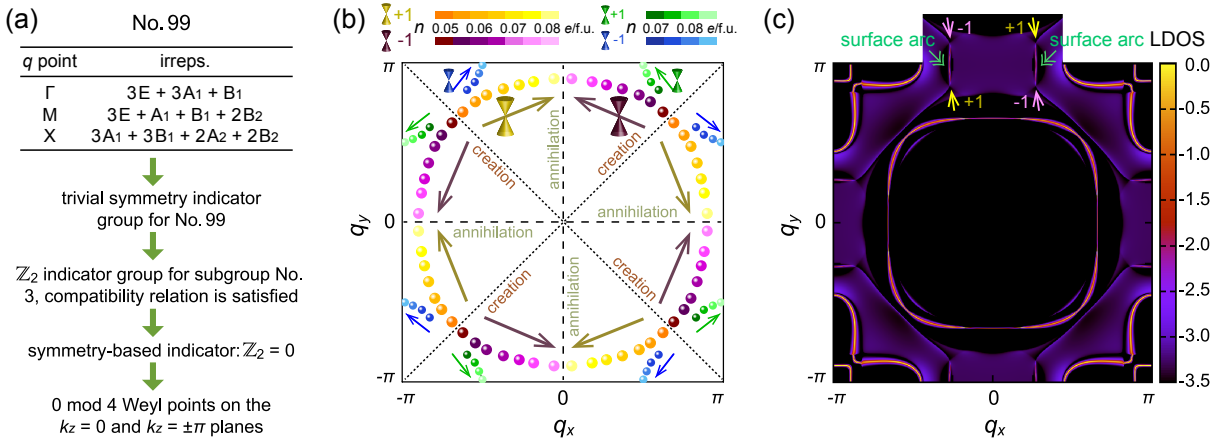


**Figure 3: Weyl points in tetragonal BaTiO<sub>3</sub> controlled by light.** (a) Diagnosis process for the eight Weyl points in BaTiO<sub>3</sub> using symmetry-based indicator theory for the lowest 10 bands. (b) Evolution of the Weyl points on the  $q_z = \pi$  plane with increasing  $n$  from 0.050 to 0.085 e/f.u. (c) Phonon surface arcs for a phonon frequency of 11.42 THz at  $n = 0.07$  e/f.u.

In addition to nodal lines and nodal rings, Weyl phonons are also sensitive to the photoexcited carrier concentration  $n$ . Fig. 3(b) shows the evolution of eight pairs of Weyl points on the  $q_z = \pi$  plane when increasing  $n$  from 0.050 to 0.085 e/f.u. (four extra pairs of Weyl points

emerge when  $0.0695 < n < 0.0825$  e/f.u.). Below 0.050 e/f.u., BaTiO<sub>3</sub> exhibits no Weyl points between the 10<sup>th</sup> and 11<sup>th</sup> branches in its phonon spectrum. At about  $n = 0.050$  e/f.u., four pairs of Weyl points are created around the  $q_x = q_y$  and  $q_x = -q_y$  planes [orange and maroon dots in Fig. 3(b)]. As  $n$  increases, the Weyl points in each pair with different chirality move away from each other and head to the  $q_x = 0$  and  $q_y = 0$  planes [yellow and purple arrows in Fig. 3(b)]. Once  $n$  reaches 0.0815 e/f.u, Weyl points meet on the  $q_x = 0$  and  $q_y = 0$  planes and annihilate in pairs [light yellow and light magenta dots in Fig. 3(b)]. In addition, another four pairs of Weyl points of opposite chirality are created around the  $q_x = q_y$  and  $q_x = -q_y$  planes at  $n = 0.0695$  e/f.u., and annihilate in pairs on the  $q_x = \pi$  and  $q_y = \pi$  planes when  $n$  reaches 0.0825 e/f.u. [blue and green dots in Fig. 3(b)]. Since no band inversion happens at any high-symmetry points in this process, the Berry phase of the loop R-A-A'-R'-R on the  $q_z = \pi$  plane remains zero, which is consistent with  $0 \bmod 4$  Weyl points on the  $q_z = \pi$  plane with  $\mathbb{Z}_2 = 0$  [Fig. 3(a)].

To have a better understanding of the Weyl phonons in tetragonal BaTiO<sub>3</sub>, we calculate the surface local density of states (LDOS) from the imaginary part of the surface Green's function (52). The surface LDOS in Fig. 3(c) is calculated along the (001) direction at 11.42 THz and  $n = 0.07$  e/f.u. The four pairs of Weyl points connect via surface arcs crossing the Brillouin zone boundaries, so that each surface arc starts from one Weyl point with a positive monopole charge and ends at another with a negative one. Overall, by modulating  $n$  we can control the creation and annihilation of Weyl points, and the length of surface arcs in tetragonal BaTiO<sub>3</sub>.

## Topological phonons in PbTiO<sub>3</sub>

Multiple types of topological phonons can also be found in other perovskites with the same  $P4mm$  space group, and here we study PbTiO<sub>3</sub> and SrTiO<sub>3</sub> as additional examples.

PbTiO<sub>3</sub> has a tetragonal  $P4mm$  structure for  $T < 600$  K, and a cubic structure above that

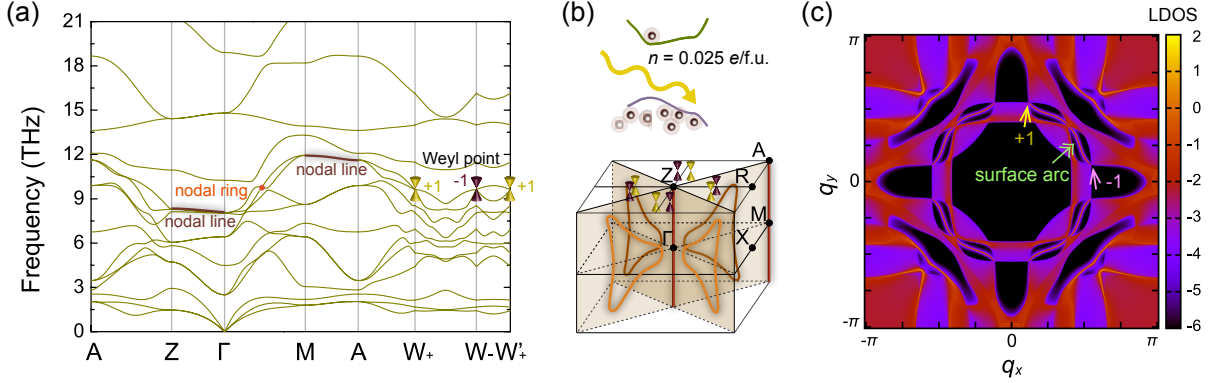


Figure 4: **Topological phonons in tetragonal  $\text{PbTiO}_3$ .** (a) Phonon dispersion of tetragonal  $P4mm$   $\text{PbTiO}_3$  at  $n = 0.025$  e/f.u. (b) Bulk Brillouin zone at  $n = 0.025$  e/f.u. with four nodal rings on the  $q_x = q_y$  and  $q_x = -q_y$  planes (orange circles), two nodal lines along the  $\Gamma$ -Z and M-A high-symmetry lines (brown line), and eight Weyl points located on  $q_z = \pi$  plane (purple and yellow cones). All these three types of topological phonons are composed by the 10<sup>th</sup> and 11<sup>th</sup> bands. (c) Phonon surface arcs for a phonon frequency of 9.63 THz at  $n = 0.025$  e/f.u.

temperature. Although the  $P4mm$  phase has the lowest energy in a wide photoexcited density range  $n < 0.125$  e/f.u. (39), it becomes dynamically unstable when  $n > 0.05$  e/f.u. (shown in the Supplementary Materials). We calculate the excited-state phonon dispersion at  $n = 0.025$  e/f.u., as shown in Fig. 4(a). Similar to  $\text{BaTiO}_3$ ,  $\text{PbTiO}_3$  also has nodal rings, nodal lines, and Weyl points between the 10<sup>th</sup> and 11<sup>th</sup> bands. But the triple Weyl points no longer exist as the nodal rings and the nodal line do not touch. The unique band crossings along the  $\Gamma$ -M high-symmetry line bring about four nodal rings on the  $q_x = q_y$  and  $q_x = -q_y$  planes protected by  $M_{xy}$  and  $M_{x\bar{y}}$  symmetries. The endless nodal lines along the  $\Gamma$ -Z and M-A directions are robust as well, as they are protected by the  $C_{4z}$  symmetry.

The surface LDOS in Fig. 4(c) is calculated along the (001) direction at 9.63 THz with  $n = 0.025$  e/f.u. Four pairs of Weyl points, created at  $n = 0.005$  e/f.u., connect with each other via surface arcs crossing the  $q_x = q_y$  and  $q_x = -q_y$  planes. We note that the location of these four pairs of Weyl points can also be modulated by changing the photoexcitation density until the lattice becomes dynamically unstable for  $n > 0.05$  e/f.u.

## Topological phonons in SrTiO<sub>3</sub>

SrTiO<sub>3</sub> has a different phase diagram compared to BaTiO<sub>3</sub> and PbTiO<sub>3</sub>. At low temperatures, it exhibits a centrosymmetric tetragonal phase of space group  $I4/mcm$ , and undergoes a phase transition to a cubic phase above 106 K. The  $P4mm$  phase can only be accessed with small negative strains (53, 54). The in-plane lattice constants  $a$  and  $b$  of  $P4mm$  SrTiO<sub>3</sub> increase upon photoexcitation. Therefore by fixing  $a$  and  $b$  to the ones in the dark, we can induce in-plane negative strain in illuminated SrTiO<sub>3</sub>. This can be realized experimentally by growing SrTiO<sub>3</sub> on an appropriate substrate. As shown in Fig. 5(a), after fixing the in-plane lattice constants  $a$  and  $b$  and relaxing only the out-of-plane lattice constant  $c$  in the  $P4mm$  phase, we find that the tetragonal phase can have a lower energy than the cubic  $Pm\bar{3}m$  phase.

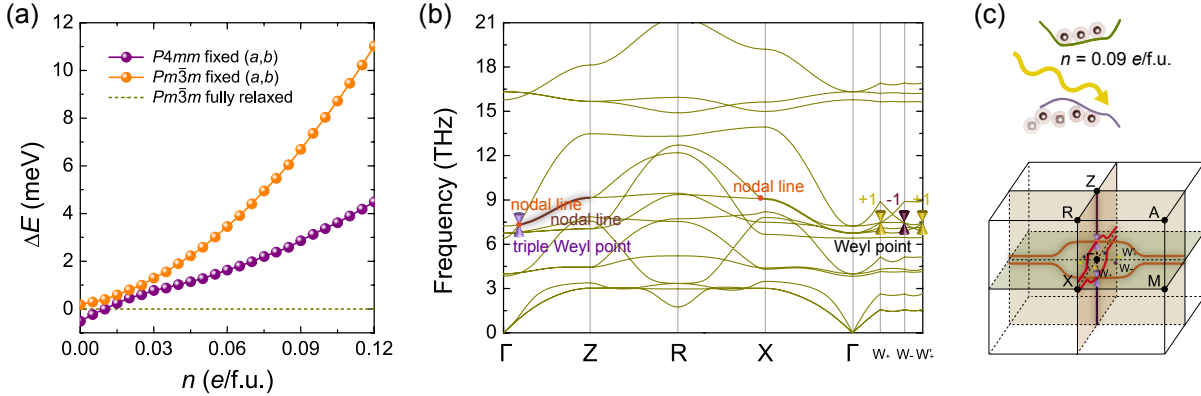


Figure 5: **Topological phonons in tetragonal SrTiO<sub>3</sub>.** (a) Relative energy difference between the  $P4mm$  and  $Pm\bar{3}m$  phases with fixed in-plane lattice constants  $a$  and  $b$ , with the energy of the fully relaxed  $Pm\bar{3}m$  phase set to be zero. (b) Phonon dispersion of tetragonal  $P4mm$  SrTiO<sub>3</sub> at  $n = 0.09$  e/f.u. (c) Bulk Brillouin zone at  $n = 0.09$  e/f.u. with two nodal lines on the  $q_x = 0$  and  $q_y = 0$  planes (orange lines), one nodal line along the  $\Gamma$ -Z high-symmetry line (brown line), one pair of triple Weyl points at the intersection points between the three nodal lines (violet cones), and four pairs of Weyl points on the  $q_z = 0$  plane (purple and yellow dots).

$P4mm$  SrTiO<sub>3</sub> exhibits imaginary phonon modes in the dark, while adding a photoexcited charge density of  $n = 0.09$  e/f.u. stabilizes the structure, as shown in Fig. 5(b). Similar to BaTiO<sub>3</sub>, the  $P4mm$  phase of SrTiO<sub>3</sub> has four nodal lines in total on the  $q_x = 0$  and  $q_y = 0$

mirror planes and one nodal line along the  $\Gamma$ -Z high-symmetry line in the bulk Brillouin zone. The intersection points of the three nodal lines form one pair of triple Weyl points. Different from  $\text{BaTiO}_3$ , the four pairs of Weyl points are located on the  $q_z = 0$  plane rather than the  $q_z = \pi$  plane. Weyl phonons in  $\text{SrTiO}_3$  can also be manipulated by photoexcitation, and the critical  $n$  for the annihilation of the Weyl points on the  $q_x = 0$  and  $q_y = 0$  planes is 0.105  $e/f.u.$ , which is similar to that in  $\text{BaTiO}_3$ .

## Ubiquity of topological phonons in perovskite oxides

The existence and coexistence of different types of topological phonons, together with their tunability by light, occur in a variety of other structural phases of perovskites beyond the tetragonal phases investigated above. Topological phonons in the orthorhombic  $Amm2$  and the rhombohedral  $R3m$  phases of  $\text{BaTiO}_3$  are shown in the Supplementary Materials. Furthermore, topological phonons in oxide perovskites can also be manipulated by other tuning parameters beyond photoexcitation, such as strain and temperature (for details, see the Supplementary Materials). Putting these insights together suggests that topological phonons are ubiquitous in the family of perovskite oxides, which, given their widespread use and versatility, provide a promising platform for exploring topological phonon physics and its interplay with other phases.

Given the proposed ubiquity of topological phonons in perovskites, it should be possible to directly identify them experimentally by looking for “isolated” band crossings, and the prototype materials detailed above are promising starting candidates. Topological bulk phonons can be measured by inelastic neutron scattering (23,55,56) and inelastic X-ray scattering (20), while the accompanying topological surface states can be detected by high resolution electron energy loss spectroscopy (57). For light-induced topological phonons, although it may be difficult to illuminate the sample to maintain a constant photoexcited carrier density, transient photoexcitation could be used to observe the evolution of nodal rings, nodal lines and Weyl points as a

function of the time-dependent photoexcited carrier density.

In terms of phenomena, topological phonons with non-zero Berry curvature may contribute to the recently observed phonon thermal Hall effect in  $\text{SrTiO}_3$  (30, 58). In addition, novel phonon-phonon and electron-phonon scattering mechanisms could arise from topological phonons, which may provide new insights on the enhanced superconductivity of  $\text{SrTiO}_3$  (26, 59). The emergence of Weyl phonons may be accompanied by other unique physical properties such as a pseudogauge field with a one-way propagating bulk mode (60–62), topological negative refraction (18), and nonlinear acoustic/optical responses (63, 64), which can offer new routes for designing novel technologies like light-controlled neuromorphic computing in phononic systems (65, 66). Our work shows that oxide perovskites provide a promising platform to explore all of these phenomena and applications.

## Conclusion

We find that topological phonons are ubiquitous in oxide perovskites and that photoexcitation provides a promising route for their manipulation. As examples, the noncentrosymmetric tetragonal phases of three oxide perovskites ( $\text{BaTiO}_3$ ,  $\text{PbTiO}_3$ , and  $\text{SrTiO}_3$ ) exhibit topological nodal rings, nodal lines, and Weyl points in their phonon spectra. Remarkably, we find that photoexcitation is the only way to obtain Weyl phonons in tetragonal  $\text{BaTiO}_3$ , since the thermally-stabilized tetragonal phase has a large LO-TO energy splitting in the phonon spectrum that prevents band crossings. By contrast, photoexcited carriers screen long-range interactions, suppressing the LO-TO energy splitting and facilitating the band crossings. We also find that the photoexcited carrier density can be used to tune the creation and annihilation of Weyl points and nodal rings/lines without any associated structural phase transitions. Topological phonons in oxide perovskites provide a promising platform to study physical phenomena ranging from the phonon Hall effect to superconductivity, and may also offer new technological opportunities

such as the realization of controllable topological quantum states for neuromorphic computing.

## Methods

Density functional theory (DFT) calculations are performed using the Vienna *ab initio* simulation package (VASP) with the projector-augmented-wave potential method (67, 68). We use the generalized gradient approximation (GGA) with the Perdew-Burke-Ernzerhof parameterization revised for solids (PBEsol) as the exchange-correlation functional (69). A plane-wave basis set is employed with a kinetic energy cutoff of 800 eV and a  $7 \times 7 \times 7$  **k**-mesh during structural relaxation, which is stopped when forces are below  $10^{-3}$  eV/Å. The band structure of BaTiO<sub>3</sub> is calculated using the HSE06 hybrid functional in the presence of spin-orbit coupling (70). Photoexcited carriers are simulated by promoting electrons from high-energy valence band states to low-energy conduction band states. This  $\Delta$  self-consistent field ( $\Delta$ SCF) method introduces non-interacting electron-hole pairs by changing the occupation numbers of the Kohn-Sham orbitals (71–74), and is computationally less demanding compared to other approaches like constrained density functional theory (75) and excited-state force calculations (76). Nevertheless, it gives consistent phonon spectra compared with those obtained with constrained DFT (39), as shown in the Supplementary Materials. The occupancies are fixed with a smearing of 0.01 eV.

The crystal structures in the dark and under photoexcitation are fully relaxed before the phonon calculations. We calculate the force constants with density functional perturbation theory (DFPT) (77) in a  $2 \times 2 \times 2$  supercell with a  $5 \times 5 \times 5$  **k**-mesh using VASP. The phonon dispersion is then obtained using PHONOPY (78). We perform convergence tests on the supercell size between  $2 \times 2 \times 2$ ,  $3 \times 3 \times 3$ , and  $4 \times 4 \times 2$ , all confirming the existence of Weyl points in illuminated BaTiO<sub>3</sub>. We calculate the chirality of Weyl points by employing the Wilson-loop method to calculate the Wannier charge center flow, *i.e.*, the monopole charge of a Weyl point (79, 80). The phonon surface states are obtained using surface Green's functions

as implemented in WANNIERTOOLS (52). The finite-temperature phonon frequencies including anharmonic contributions are calculated using a self-consistent *ab initio* lattice dynamical method (45, 81, 82) in a  $2 \times 2 \times 2$  supercell. The self-consistent cycle is terminated after 240 iterations when the difference in free energy is less than 0.2 meV, and the space group symmetry is enforced on the resulting force constants. The Born effective charges are calculated using DFPT to obtain the LO-TO splitting in the phonon dispersion in the dark (83). Under illumination, the photoexcited electrons screen long-range interactions and no LO-TO splitting occurs.

## References

1. T. T. Heikkilä, N. B. Kopnin, G. E. Volovik, Flat bands in topological media, *JETP Letters* **94**, 233– (2011).
2. D. T. Son, B. Z. Spivak, Chiral anomaly and classical negative magnetoresistance of weyl metals, *Phys. Rev. B* **88**, 104412 (2013).
3. J. Xiong, S. K. Kushwaha, T. Liang, J. W. Krizan, M. Hirschberger, W. Wang, R. J. Cava, N. P. Ong, Evidence for the chiral anomaly in the Dirac semimetal  $\text{Na}_3\text{Bi}$ , *Science* **350**, 413 (2015).
4. H. Weng, Y. Liang, Q. Xu, R. Yu, Z. Fang, X. Dai, Y. Kawazoe, Topological node-line semimetal in three-dimensional graphene networks, *Phys. Rev. B* **92**, 045108 (2015).
5. A. Bernevig, H. Weng, Z. Fang, X. Dai, Recent Progress in the Study of Topological Semimetals, *J. Phys. Soc. Jpn.* **87**, 041001 (2018).
6. C. Fang, Y. Chen, H.-Y. Kee, L. Fu, Topological nodal line semimetals with and without spin-orbital coupling, *Phys. Rev. B* **92**, 081201 (2015).



7. Z. Wang, Y. Sun, X.-Q. Chen, C. Franchini, G. Xu, H. Weng, X. Dai, Z. Fang, Dirac semimetal and topological phase transitions in  $A_3\text{Bi}$  ( $A = \text{Na, K, Rb}$ ), *Phys. Rev. B* **85**, 195320 (2012).
8. N. P. Armitage, E. J. Mele, A. Vishwanath, Weyl and Dirac semimetals in three-dimensional solids, *Rev. Mod. Phys.* **90**, 015001 (2018).
9. S.-Y. Xu, I. Belopolski, N. Alidoust, M. Neupane, G. Bian, C. Zhang, R. Sankar, G. Chang, Z. Yuan, C.-C. Lee, S.-M. Huang, H. Zheng, J. Ma, D. S. Sanchez, B. Wang, A. Bansil, F. Chou, P. P. Shibayev, H. Lin, S. Jia, M. Z. Hasan, Discovery of a weyl fermion semimetal and topological fermi arcs, *Science* **349**, 613–617 (2015).
10. H. Weng, C. Fang, Z. Fang, B. A. Bernevig, X. Dai, Weyl semimetal phase in noncentrosymmetric transition-metal monophosphides, *Phys. Rev. X* **5**, 011029 (2015).
11. L. X. Yang, Z. K. Liu, Y. Sun, H. Peng, H. F. Yang, T. Zhang, B. Zhou, Y. Zhang, Y. F. Guo, M. Rahn, D. Prabhakaran, Z. Hussain, S.-K. Mo, C. Felser, B. Yan, Y. L. Chen, Weyl semimetal phase in the non-centrosymmetric compound taas, *Nat Phys* **11**, 728–732 (2015).
12. S.-Y. Yang, H. Yang, E. Derunova, S. S. P. Parkin, B. Yan, M. N. Ali, Symmetry demanded topological nodal-line materials, *Advances in Physics: X* **3**, 1414631– (2018).
13. J. He, X. Li, P. Lyu, P. Nachtigall, Near-room-temperature chern insulator and dirac spin-gapless semiconductor: nickel chloride monolayer, *Nanoscale* **9**, 2246–2252 (2017).
14. F. Wu, T. Lovorn, A. H. MacDonald, Topological exciton bands in moiré heterojunctions, *Phys. Rev. Lett.* **118**, 147401 (2017).
15. F.-Y. Li, Y.-D. Li, Y. B. Kim, L. Balents, Y. Yu, G. Chen, Weyl magnons in breathing pyrochlore antiferromagnets, *Nature Communications* **7**, 12691– (2016).

16. O. Stenull, C. L. Kane, T. C. Lubensky, Topological phonons and weyl lines in three dimensions, *Phys. Rev. Lett.* **117**, 068001 (2016).
17. Y. Liu, Y. Xu, S.-C. Zhang, W. Duan, Model for topological phononics and phonon diode, *Phys. Rev. B* **96**, 064106 (2017).
18. H. He, C. Qiu, L. Ye, X. Cai, X. Fan, M. Ke, F. Zhang, Z. Liu, Topological negative refraction of surface acoustic waves in a weyl phononic crystal, *Nature* **560**, 61–64 (2018).
19. T. Zhang, Z. Song, A. Alexandradinata, H. Weng, C. Fang, L. Lu, Z. Fang, Double-weyl phonons in transition-metal monosilicides, *Phys. Rev. Lett.* **120**, 016401 (2018).
20. H. Miao, T. T. Zhang, L. Wang, D. Meyers, A. H. Said, Y. L. Wang, Y. G. Shi, H. M. Weng, Z. Fang, M. P. M. Dean, Observation of double weyl phonons in parity-breaking fesi, *Phys. Rev. Lett.* **121**, 035302 (2018).
21. J. Li, Q. Xie, S. Ullah, R. Li, H. Ma, D. Li, Y. Li, X.-Q. Chen, Coexistent three-component and two-component weyl phonons in tis, zrse, and hfte, *Phys. Rev. B* **97**, 054305 (2018).
22. B. W. Xia, R. Wang, Z. J. Chen, Y. J. Zhao, H. Xu, Symmetry-protected ideal type-ii weyl phonons in cdte, *Phys. Rev. Lett.* **123**, 065501 (2019).
23. T. T. Zhang, H. Miao, Q. Wang, J. Q. Lin, Y. Cao, G. Fabbri, A. H. Said, X. Liu, H. C. Lei, Z. Fang, H. M. Weng, M. P. M. Dean, Phononic helical nodal lines with  $\mathcal{PT}$  protection in  $\text{mob}_2$ , *Phys. Rev. Lett.* **123**, 245302 (2019).
24. Y. Liu, X. Chen, Y. Xu, Topological phononics: From fundamental models to real materials, *Adv. Funct. Mater.* **30**, 1904784– (2020).

25. A. P. Drozdov, M. I. Erements, I. A. Troyan, V. Ksenofontov, S. I. Shylin, Conventional superconductivity at 203 kelvin at high pressures in the sulfur hydride system, *Nature* **525**, 73–76 (2015).
26. K. Ahadi, L. Galletti, Y. Li, S. Salmani-Rezaie, W. Wu, S. Stemmer, Enhancing superconductivity in  $\text{SrTiO}_3$  films with strain, *Sci Adv* **5**, eaaw0120– (2019).
27. S. Murakami, A. Okamoto, Thermal hall effect of magnons, *J. Phys. Soc. Jpn.* **86**, 011010– (2016).
28. J.-Y. Chen, S. A. Kivelson, X.-Q. Sun, Enhanced thermal hall effect in nearly ferroelectric insulators, *Phys. Rev. Lett.* **124**, 167601 (2020).
29. M. Hamada, S. Murakami, Phonon rotoelectric effect, *Phys. Rev. B* **101**, 144306 (2020).
30. X. Li, B. Fauqué, Z. Zhu, K. Behnia, Phonon thermal hall effect in strontium titanate, *Phys. Rev. Lett.* **124**, 105901 (2020).
31. R. E. Cohen, Origin of ferroelectricity in perovskite oxides, *Nature* **358**, 136–138 (1992).
32. Y. Moritomo, H. Kuwahara, Y. Tomioka, Y. Tokura, Pressure effects on charge-ordering transitions in perovskite manganites, *Phys. Rev. B* **55**, 7549–7556 (1997).
33. Y. Nahas, S. Prokhorenko, L. Louis, Z. Gui, I. Kornev, L. Bellaiche, Discovery of stable skyrmionic state in ferroelectric nanocomposites, *Nature Communications* **6**, 8542– (2015).
34. S. Das, Y. L. Tang, Z. Hong, M. A. P. Goncalves, M. R. McCarter, C. Klewe, K. X. Nguyen, F. Gómez-Ortiz, P. Shafer, E. Arenholz, V. A. Stoica, S.-L. Hsu, B. Wang, C. Ophus, J. F. Liu, C. T. Nelson, S. Saremi, B. Prasad, A. B. Mei, D. G. Schlom, J. Íñiguez, P. García-Fernández, D. A. Muller, L. Q. Chen, J. Junquera, L. W. Martin, R. Ramesh, Observation of room-temperature polar skyrmions, *Nature* **568**, 368–372 (2019).

35. A. Mahmoud, A. Erba, K. E. El-Kelany, M. Rérat, R. Orlando, Low-temperature phase of  $\text{BaTiO}_3$ : Piezoelectric, dielectric, elastic, and photoelastic properties from ab initio simulations, *Phys. Rev. B* **89**, 045103 (2014).
36. K. H. Ahn, T. Lookman, A. R. Bishop, Strain-induced metal-insulator phase coexistence in perovskite manganites, *Nature* **428**, 401–404 (2004).
37. Y. Shirako, H. Kojitani, M. Akaogi, K. Yamaura, E. Takayama-Muromachi, High-pressure phase transitions of  $\text{CaTiO}_3$  perovskite, *Physics and Chemistry of Minerals* **36**, 455– (2009).
38. L. L. Rusevich, G. Zvejnieks, E. A. Kotomin, M. M. Krzmann, A. Meden, S. Kunej, I. D. Vlaicu, Theoretical and experimental study of  $(\text{Ba},\text{Sr})\text{TiO}_3$  perovskite solid solutions and  $\text{BaTiO}_3/\text{SrTiO}_3$  heterostructures, *J. Phys. Chem. C* **123**, 2031–2036 (2019).
39. C. Paillard, E. Torun, L. Wirtz, J. Íñiguez, L. Bellaiche, Photoinduced phase transitions in ferroelectrics, *Phys. Rev. Lett.* **123**, 087601 (2019).
40. T. F. Nova, A. S. Disa, M. Fechner, A. Cavalleri, Metastable ferroelectricity in optically strained  $\text{SrTiO}_3$ , *Science* **364**, 1075– (2019).
41. Y. Ahn, A. Pateras, S. D. Marks, H. Xu, T. Zhou, Z. Luo, Z. Chen, L. Chen, X. Zhang, A. D. DiChiara, H. Wen, P. G. Evans, Nanosecond optically induced phase transformation in compressively strained  $\text{BiFeO}_3$  on  $\text{LaAlO}_3$ , *Phys. Rev. Lett.* **123**, 045703 (2019).
42. M. Porer, M. Fechner, M. Kubli, M. J. Neugebauer, S. Parchenko, V. Esposito, A. Narayan, N. A. Spaldin, R. Huber, M. Radovic, E. M. Bothschafter, J. M. Glownia, T. Sato, S. Song, S. L. Johnson, U. Staub, Ultrafast transient increase of oxygen octahedral rotations in a perovskite, *Phys. Rev. Research* **1**, 012005 (2019).

43. D. M. Juraschek, M. Fechner, N. A. Spaldin, Ultrafast structure switching through nonlinear phononics, *Phys. Rev. Lett.* **118**, 054101 (2017).
44. H. F. KAY, R. G. RHODES, Barium titanate crystals, *Nature* **160**, 126–127 (1947).
45. P. Souvatzis, O. Eriksson, M. I. Katsnelson, S. P. Rudin, Entropy driven stabilization of energetically unstable crystal structures explained from first principles theory, *Phys. Rev. Lett.* **100**, 095901 (2008).
46. C. Fang, H. Weng, X. Dai, Z. Fang, Topological nodal line semimetals, *Chinese Physics B* **25**, 117106– (2016).
47. H. C. Po, A. Vishwanath, H. Watanabe, Symmetry-based indicators of band topology in the 230 space groups, *Nature Communications* **8**, 50– (2017).
48. Z. Song, T. Zhang, C. Fang, Diagnosis for nonmagnetic topological semimetals in the absence of spin-orbital coupling, *Phys. Rev. X* **8**, 031069 (2018).
49. J. Kruthoff, J. de Boer, J. van Wezel, C. L. Kane, R.-J. Slager, Topological classification of crystalline insulators through band structure combinatorics, *Phys. Rev. X* **7**, 041069 (2017).
50. T. Zhang, L. Lu, S. Murakami, Z. Fang, H. Weng, C. Fang, Diagnosis scheme for topological degeneracies crossing high-symmetry lines, *Phys. Rev. Research* **2**, 022066 (2020).
51. W. Zhong, R. D. King-Smith, D. Vanderbilt, Giant lo-to splittings in perovskite ferroelectrics, *Phys. Rev. Lett.* **72**, 3618–3621 (1994).
52. Q. Wu, S. Zhang, H.-F. Song, M. Troyer, A. A. Soluyanov, WannierTools: An open-source software package for novel topological materials, *Computer Physics Communications* **224**, 405–416 (2018).

53. O. Diéguez, K. M. Rabe, D. Vanderbilt, First-principles study of epitaxial strain in perovskites, *Phys. Rev. B* **72**, 144101 (2005).
54. L. Ni, Y. Liu, C. Song, W. Wang, G. Han, Y. Ge, First-principle study of strain-driven phase transition in incipient ferroelectric  $\text{SrTiO}_3$ , *Physica B: Condensed Matter* **406**, 4145–4149 (2011).
55. X. He, D. Bansal, B. Winn, S. Chi, L. Boatner, O. Delaire, Anharmonic eigenvectors and acoustic phonon disappearance in quantum paraelectric  $\text{SrTiO}_3$ , *Phys. Rev. Lett.* **124**, 145901 (2020).
56. N. Choudhury, E. J. Walter, A. I. Kolesnikov, C.-K. Loong, Large phonon band gap in  $\text{SrTiO}_3$  and the vibrational signatures of ferroelectricity in  $a\text{TiO}_3$  perovskites: First-principles lattice dynamics and inelastic neutron scattering, *Phys. Rev. B* **77**, 134111 (2008).
57. X. Jia, S. Zhang, R. Sankar, F.-C. Chou, W. Wang, K. Kempa, E. W. Plummer, J. Zhang, X. Zhu, J. Guo, Anomalous acoustic plasmon mode from topologically protected states, *Phys. Rev. Lett.* **119**, 136805 (2017).
58. Y.-f. Yang, G.-M. Zhang, F.-C. Zhang, Universal behavior of the thermal hall conductivity, *Phys. Rev. Lett.* **124**, 186602 (2020).
59. J. J. Lee, F. T. Schmitt, R. G. Moore, S. Johnston, Y.-T. Cui, W. Li, M. Yi, Z. K. Liu, M. Hashimoto, Y. Zhang, D. H. Lu, T. P. Devereaux, D.-H. Lee, Z.-X. Shen, Interfacial mode coupling as the origin of the enhancement of  $t_c$  in fese films on  $\text{SrTiO}_3$ , *Nature* **515**, 245–248 (2014).
60. S. Roy, M. Kolodrubetz, N. Goldman, A. G. Grushin, Tunable axial gauge fields in engineered weyl semimetals: semiclassical analysis and optical lattice implementations, *2D Materials* **5**, 024001– (2018).

61. H. Jia, R. Zhang, W. Gao, Q. Guo, B. Yang, J. Hu, Y. Bi, Y. Xiang, C. Liu, S. Zhang, Observation of chiral zero mode in inhomogeneous three-dimensional weyl metamaterials, *Science* **363**, 148– (2019).
62. V. Peri, M. Serra-Garcia, R. Ilan, S. D. Huber, Axial-field-induced chiral channels in an acoustic weyl system, *Nature Physics* **15**, 357–361 (2019).
63. J. Kim, K.-W. Kim, D. Shin, S.-H. Lee, J. Sinova, N. Park, H. Jin, Prediction of ferroelectricity-driven berry curvature enabling charge- and spin-controllable photocurrent in tin telluride monolayers, *Nature Communications* **10**, 3965– (2019).
64. P. O. Sukhachov, H. Rostami, Acoustogalvanic effect in dirac and weyl semimetals, *Phys. Rev. Lett.* **124**, 126602 (2020).
65. N. Farmakidis, N. Youngblood, X. Li, J. Tan, J. L. Swett, Z. Cheng, C. D. Wright, W. H. P. Pernice, H. Bhaskaran, Plasmonic nanogap enhanced phase-change devices with dual electrical-optical functionality, *Sci Adv* **5**, eaaw2687– (2019).
66. J. Feldmann, N. Youngblood, C. D. Wright, H. Bhaskaran, W. H. P. Pernice, All-optical spiking neurosynaptic networks with self-learning capabilities, *Nature* **569**, 208–214 (2019).
67. G. Kresse, J. Furthmüller, Efficient iterative schemes for *ab initio* total-energy calculations using a plane-wave basis set, *Phys. Rev. B* **54**, 11169–11186 (1996).
68. G. Kresse, J. Furthmüller, Efficiency of ab-initio total energy calculations for metals and semiconductors using a plane-wave basis set, *Computational Materials Science* **6**, 15 - 50 (1996).

69. J. P. Perdew, A. Ruzsinszky, G. I. Csonka, O. A. Vydrov, G. E. Scuseria, L. A. Constantin, X. Zhou, K. Burke, Restoring the Density-Gradient Expansion for Exchange in Solids and Surfaces, *Phys. Rev. Lett.* **100**, 136406 (2008).
70. J. Heyd, G. E. Scuseria, M. Ernzerhof, Hybrid functionals based on a screened Coulomb potential, *J. Chem. Phys.* **118**, 8207 (2003).
71. R. O. Jones, O. Gunnarsson, The density functional formalism, its applications and prospects, *Rev. Mod. Phys.* **61**, 689–746 (1989).
72. A. Görling, Density-functional theory for excited states, *Phys. Rev. A* **54**, 3912–3915 (1996).
73. A. Hellman, B. Razaznejad, B. I. Lundqvist, Potential-energy surfaces for excited states in extended systems, *J. Chem. Phys.* **120**, 4593–4602 (2004).
74. B. Peng, H. Zhang, W. Chen, B. Hou, Z.-J. Qiu, H. Shao, H. Zhu, B. Monserrat, D. Fu, H. Weng, C. M. Soukoulis, Sub-picosecond photo-induced displacive phase transition in two-dimensional mote2, *npj 2D Materials and Applications* **4**, 14– (2020).
75. F. Mauri, R. Car, First-principles study of excitonic self-trapping in diamond, *Phys. Rev. Lett.* **75**, 3166–3169 (1995).
76. S. Ismail-Beigi, S. G. Louie, Excited-state forces within a first-principles green’s function formalism, *Phys. Rev. Lett.* **90**, 076401 (2003).
77. S. Baroni, S. de Gironcoli, A. Dal Corso, P. Giannozzi, Phonons and related crystal properties from density-functional perturbation theory, *Rev. Mod. Phys.* **73**, 515-562 (2001).
78. A. Togo, I. Tanaka, First principles phonon calculations in materials science, *Scripta Materialia* **108**, 1-5 (2015).



79. A. A. Soluyanov, D. Vanderbilt, Computing topological invariants without inversion symmetry, *Phys. Rev. B* **83**, 235401 (2011).
80. R. Yu, X. L. Qi, A. Bernevig, Z. Fang, X. Dai, Equivalent expression of  $F_2$  topological invariant for band insulators using the non-abelian berry connection, *Phys. Rev. B* **84**, 075119 (2011).
81. D. Alfè, Phon: A program to calculate phonons using the small displacement method, *Computer Physics Communications* **180**, 2622–2633 (2009).
82. B. Cai, X. Chen, M. Xie, S. Zhang, X. Liu, J. Yang, W. Zhou, S. Guo, H. Zeng, A class of pb-free double perovskite halide semiconductors with intrinsic ferromagnetism, large spin splitting and high curie temperature, *Mater. Horiz.* **5**, 961–968 (2018).
83. M. Gajdoš, K. Hummer, G. Kresse, J. Furthmüller, F. Bechstedt, Linear optical properties in the projector-augmented wave methodology, *Phys. Rev. B* **73**, 045112 (2006).

## Acknowledgments

The authors gratefully acknowledge helpful discussions with Danny Bennett (University of Cambridge) on the phase diagram of oxide perovskites, Prof. Guntars Zvejnieks (University of Latvia) on the crystal structures of BaTiO<sub>3</sub>, Bowen Hou and Prof. Hao Zhang (Fudan University) on the  $\Delta$ SCF method, Dr Bo Cai (Nanjing University of Science and Technology) on finite-temperature lattice dynamics, and Prof. Stefano Baroni (SISSA) on the screening effect of photoexcited carriers. B.P. and B.M. acknowledge support from the Winton Programme for the Physics of Sustainability, and B.M. also acknowledges support from the Gianna Angelopoulos Programme for Science, Technology, and Innovation. Y.H. acknowledges support from EPSRC grant EP/R512461/1 and Trinity College Henry-Barlow Scholarship. S.M. and T.T.Z.

acknowledge support from the Tokodai Institute for Element Strategy (TIES) funded by MEXT Elements Strategy Initiative to Form Core Research Center, and S.M. also acknowledges support by JSPS KAKENHI Grant Number JP18H03678. The calculations were performed using resources provided by the Cambridge Tier-2 system operated by the University of Cambridge Research Computing Service (<http://www.hpc.cam.ac.uk>) and funded by EPSRC Tier-2 capital grant EP/P020259/1, and also with computational support from the UK Materials and Molecular Modelling Hub, which is partially funded by EPSRC (EP/P020194), for which access was obtained via the UKCP consortium and funded by EPSRC grant ref EP/P022561/1.

**Competing Interests:** The authors declare that they have no competing interests.

**Author Contributions:** B.M., T.T.Z. and B.P. devised the project idea. B.P., Y.H. and T.T.Z. performed the calculations. B.P, T.T.Z. and B.M. prepared the main part of the manuscript. B.P., Y.H., S.M., T.T.Z. and B.M. discussed the results and the ideas for their analysis and edited the manuscript.

**Data Availability:** All data needed to evaluate the conclusions in the paper are present in the paper and/or the Supplementary Materials. Additional data related to this paper may be requested from the authors.

## Supplementary materials

Supplementary Text

Figs. S1 to S9